International Tables for Crystallography (2018). Vol. H, Chapter 3.3, pp. 263–269.

3.3. Powder diffraction peak profiles

R. B. Von Dreele

3.3.1. Introduction

The analysis of a powder diffraction pattern usually involves the fitting of a model to the set of peaks that are found in that pattern. The desired result may be accurate peak positions to be used as input for an indexing procedure, or extraction of the suite of reflection intensities for crystal structure determination or a Rietveld refinement. In any case, a good description of the shape of the powder peak profile and how it varies across the entire pattern is of paramount importance for obtaining the highest-quality results, and this topic was briefly reviewed in Volume C of *International Tables for Crystallography* (Parrish, 1992).

The fitting is a least-squares procedure in which the model used to calculate the intensity of the profile is

$$Y(x) = \sum_j I_j P_j(\Delta) + B(x), \tag{3.3.1}$$

where I_j is the integrated intensity of the jth peak and P is the shape function for that peak, which depends on the offset ($\Delta = x - T_j$) of its position T_j from the observation point x. The sum is over all reflections that could contribute to the profile and $B(x)$ is a background intensity function. The observed shape of the peaks arises from a convolution of the intrinsic source profile (G_λ), the various instrumental profile contributions (G_I) (*e.g.* from slits and monochromators, discussed in Chapter 3.1) and the characteristics of the sample (G_S) that broaden the idealized reciprocal-space points (see Chapter 3.6):

$$P(\Delta) = G_\lambda * G_I * G_S. \tag{3.3.2}$$

In practice, the peak profile function is usually developed by either selecting a peak-shape function that has the required shape characteristics to fit the experimental peak profiles (the semi-empirical function approach, or SFA) or by selecting a number of contributing functions and doing the requisite convolutions (the fundamental parameters approach, or FPA) (Cheary & Coelho, 1998*b*).

Both approaches have been used for the analysis of constant-wavelength neutron and X-ray powder diffraction data and for neutron time-of-flight (energy-dispersive) powder data. In addition, the peaks can be seen to be displaced from their expected positions given by Bragg's law. As we will see, this displacement is partially a consequence of some geometric features of the experiment but is also dependent upon the particular description of the peak profile.

3.3.2. Peak profiles for constant-wavelength radiation (X-rays and neutrons)

3.3.2.1. *Introduction – symmetric peak profiles*

The realization that the neutron powder diffractometer at the Reactor Centrum Nederland, Petten, produced powder peak profiles that were Gaussian in shape led Rietveld (1967) to develop a full-pattern method for crystal structure refinement (Rietveld, 1967, 1969), now known as the Rietveld refinement method. The Gaussian is formulated as

$$P_G(\Delta, \Gamma_G \text{ or } \sigma^2) = \frac{(8\ln 2)^{1/2}}{\Gamma_G(2\pi)^{1/2}} \exp\left(\frac{-4\ln 2\Delta^2}{\Gamma_G^2}\right) = \frac{1}{(2\pi\sigma^2)^{1/2}} \exp\left(\frac{-\Delta^2}{2\sigma^2}\right), \tag{3.3.3}$$

where the width of the peak is expressed as either the full width at half-maximum (FWHM = Γ_G) or as the variance (σ^2). Rietveld also recognized the earlier analysis of the resolution of a neutron powder diffractometer by Caglioti *et al.* (1958), who showed that the contributions from the source size, collimators and monochromator crystal mosaic spread and scattering angle could be combined analytically to give

$$\Gamma_G^2 = U\tan^2\theta + V\tan\theta + W \tag{3.3.4}$$

with U, V and W adjustable during the Rietveld refinement. A modified form of this may have more stability in refinement (attributed to E. Prince by Young & Wiles, 1982):

$$\Gamma_G^2 = U'(\tan\theta - K_0)^2 + V'(\tan\theta - K_0) + W', \tag{3.3.5}$$

where K_0 is arbitrarily chosen as 0.6.

Improvements in the resolution of neutron powder diffractometers and (more importantly) attempts to apply the Rietveld method to X-ray powder diffraction data required the development of new powder profile functions (Malmros & Thomas, 1977; Young *et al.*, 1977; Young & Wiles, 1982); this is because the Gaussian function [equation (3.3.3)] gave poor fits to observed peak profiles, partially because of the Lorentzian emission line profile (G_λ) from laboratory X-ray tubes. Many functions were considered, including Lorentzian ('Cauchy'), various modified Lorentzians, Pearson VII and pseudo-Voigt. Of these the last two performed (on individual peak fits) about equally well; functional forms are:

Lorentzian 'Cauchy' function

$$P_L(\Delta, \Gamma_L) = \left(\frac{\Gamma_L}{2\pi}\right)\left\{\frac{4}{\left[\Gamma_L^2 + (2\Delta)^2\right]}\right\}, \tag{3.3.6}$$

Pearson VII function

$$P_{\text{P7}}(\Delta, \xi, \mu) = \frac{\Gamma(\mu)}{\xi\Gamma\left(\mu - \frac{1}{2}\right)(\mu\pi)^{1/2}} \Big/ \left(1 + \frac{\Delta^2}{\mu\xi^2}\right)^{\mu}, \tag{3.3.7}$$

pseudo-Voigt function

$$P_{\text{PV}}(\Delta, \Gamma, \eta) = \eta P_L(\Delta, \Gamma) + (1 - \eta)P_G(\Delta, \Gamma), \tag{3.3.8}$$

where Γ_L is the FWHM of the Lorentzian peak and $\Gamma(\mu)$ in the Pearson VII function is the Gamma function; μ may vary between 0 and ∞, and μ is the half width at $(1 + 1/\mu)^{-\mu}$ of the peak height (David, 1986); $P_{\text{P7}}(\Delta, \Gamma, 1) \simeq P_L(\Delta, \Gamma)$ and $P_{\text{P7}}(\Delta, \Gamma, \infty) \simeq P_G(\Delta, \Gamma)$. Although the Pearson VII function performs well in individual peak fits, it is of little use for Rietveld refinements because of the difficulty in relating its coefficients to physically meaningful characteristics of the sample and will not be considered further in this discussion.

The pseudo-Voigt function is an approximation to the Voigt function, which is the convolution of a Gaussian and a Lorentzian:

Voigt function

$$P_V(\Delta, \Gamma_L, \Gamma_G) = \int_{-\infty}^{\infty} P_L(\Delta, \Gamma_l) P_G(\Delta - \delta, \Gamma_G)\, \mathrm{d}\delta = \left(\frac{4 \ln 2}{\pi \Gamma_G^2}\right)^{1/2} \mathrm{Re}[\exp(-z^2)\mathrm{erfc}(-iz)], \quad (3.3.9)$$

where $z = \alpha + i\beta$, $\alpha = (4 \ln 2)^{1/2} \Delta / \Gamma_G$ and $\beta = (\ln 2)^{1/2} \Gamma_L / \Gamma_G$.

A number of formulations have been proposed for the pseudo-Voigt coefficients to make the best fit to the corresponding Voigt function (Hastings *et al.*, 1984; David, 1986; Thompson *et al.*, 1987). The latter is most commonly used and gives overall the FWHM, Γ and the mixing coefficient, η, to be used in equation (3.3.8) as functions of the individual FWHMs Γ_G and Γ_L:

$$\Gamma = [(\Gamma_G^5 + 2.69269\Gamma_G^4\Gamma_L + 2.42843\Gamma_G^3\Gamma_L^2 + 4.47163\Gamma_G^2\Gamma_L^3 + 0.07842\Gamma_G\Gamma_L^4 + \Gamma_L^5)]^{1/5}, \quad (3.3.10)$$

$$\eta = 1.36603(\Gamma_L/\Gamma) - 0.47719(\Gamma_L/\Gamma)^2 + 0.11116(\Gamma_L/\Gamma)^3. \quad (3.3.11)$$

The alternative given by David (1986) uses a more generalized version of the pseudo-Voigt function,

$$\begin{aligned} P_{\mathrm{PV}}(\Delta, W_G, W_L, \eta_G, \eta_L) &= \eta_L P_L(\Delta, W_L) + \eta_G P_G(\Delta, W_G), \\ \eta_G &= 0.00268\rho_1 + 0.75458\rho_1^2 + 2.88898\rho_1^3 - 3.85144\rho_1^4 \\ &\quad - 0.55765\rho_1^5 + 3.03824\rho_1^6 - 1.27539\rho_1^7, \\ \eta_L &= 1.35248\rho_2 + 0.41168\rho_2^2 - 2.18731\rho_2^3 + 6.42452\rho_2^4 \\ &\quad - 10.29036\rho_2^5 + 6.88093\rho_2^6 - 1.59194\rho_2^7, \\ W_G &= \Gamma(1 - 0.50734\rho_2 - 0.22744\rho_2^2 + 1.63804\rho_2^3 \\ &\quad - 2.28532\rho_2^4 + 1.31943\rho_2^5), \\ W_L &= \Gamma(1 - 0.99725\rho_1 + 1.14594\rho_1^2 + 2.56150\rho_1^3 \\ &\quad - 6.52088\rho_1^4 + 5.82647\rho_1^5 - 1.91086\rho_1^6), \end{aligned} \quad (3.3.12)$$

where $\Gamma = \Gamma_G + \Gamma_L$, $\rho_1 = \Gamma_G/\Gamma$ and $\rho_2 = \Gamma_L/\Gamma$; this is claimed to match the Voigt function to better than 0.3%.

3.3.2.2. *Constant-wavelength powder profile asymmetry*

Rietveld (1969) noted that at very low scattering angles the peaks displayed some asymmetry, which shifted the peak maximum to lower angles. He ascribed the effect to 'vertical divergence' and proposed a purely empirical correction for it. Subsequent authors (Cooper & Sayer, 1975; Howard, 1982; Hastings *et al.*, 1984) offered semi-empirical treatments of the profile shape that results from the intersection of a Debye–Scherrer cone with a finite receiving slit, which is described as 'axial divergence'. A more complete analysis of the problem in neutron powder diffraction was offered by van Laar & Yelon (1984), who considered the effect of a finite vertical slit ($2H$) intercepting a set of Bragg diffraction cones generated from a finite sample length ($2S$) within the incident beam for a goniometer radius (L). As seen in Fig. 3.3.1, this gives peak intensity beginning at $2\varphi_{\min} < 2\theta$ *via* scattering from only the ends of the sample; at $2\varphi_{\mathrm{infl}}$ the entire sample scatters into the detector. The resulting intensity profile is then convoluted with a Gaussian function to give the resulting asymmetric powder line profile (Fig. 3.3.2). This approach was then considered by Finger *et al.* (1994) for synchrotron powder diffraction and they created a Fortran code that was subsequently adopted *via* convolution with a pseudo-Voigt function [equation (3.3.12)] for use by many Rietveld refinement codes. Although originally formulated for parallel-beam neutron optics, it was shown by Finger *et al.* (1994) that it could be equally well applied to diverging X-ray and neutron optics by allowing the sample length to vary during the Rietveld refinement. They also showed that it could be applied to the asymmetry observed at low angles with Bragg–Brentano instrumentation. In that case the detector height is defined by the diffracted-beam Soller slits.

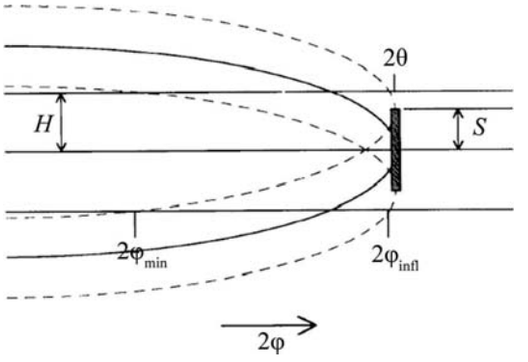

Figure 3.3.1
The band of intensity diffracted by a sample with height $2S$, as seen by a detector with opening $2H$ and a detector angle 2φ moving in the detector cylinder. For angles below $2\varphi_{\min}$ no intensity is seen. For angles between $2\varphi_{\mathrm{infl}}$ and 2θ, scattering from the entire sample can be seen by the detector. Figure and caption adapted from Finger *et al.* (1994).

Clearly, this asymmetric peak-shape function properly represents the offset of the peak top from the peak position, in contrast to functions such as the split Pearson VII function. Consequently, single peak fits using this function will give peak positions that are more readily indexed using methods such as those described in Chapter 3.4.

3.3.2.3. *Peak-displacement effects*

The position of the peak is also affected by various instrumental and geometric effects. For example, the sample position in a Bragg–Brentano experiment is ideally tangent to the focusing circle (Parrish, 1992). A radial displacement, s, of the sample will shift the Bragg peaks according to

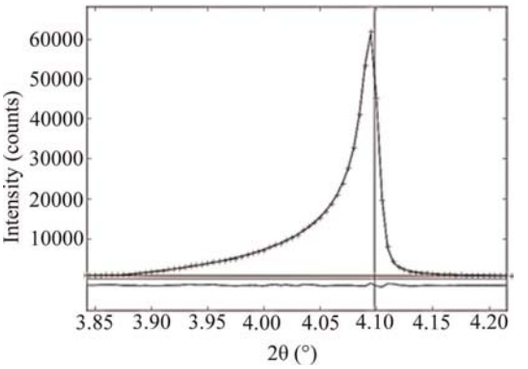

Figure 3.3.2
Low-angle synchrotron powder diffraction line ($2\theta \simeq 4.1^\circ$) fitted by the Finger *et al.* (1994) axial divergence powder line-shape function. The observed points (+), calculated curve, background and difference curves are shown. Note the offset of the peak top from the Bragg 2θ position (vertical line).

$$\Delta 2\theta = 360 s \cos\theta / \pi R, \tag{3.3.13}$$

where R is the goniometer radius. This is the major peak-displacement effect and can be detected for sample displacements as small as 10 μm.

A similar effect can be observed for Debye–Scherrer instrumentation when the goniometer axis is not coincident with the sample axis; this is a more common problem for neutron powder diffraction instruments where accurate placement of very massive goniometers can be difficult. In this case the peak displacement is

$$\Delta 2\theta = \frac{180}{\pi R}(s_x \cos 2\theta + s_y \sin 2\theta), \tag{3.3.14}$$

where s_x and s_y are displacements perpendicular and parallel to the incident beam, respectively, all in the diffraction plane.

In high-resolution instrumentation (even at a synchrotron) goniometer axis displacements less than 10 μm can be detected.

Specimen transparency in Bragg–Brentano diffraction can also cause peak displacements arising from the shift in effective sample position to below the surface at high scattering angles. This shift for a thick specimen is

$$\Delta 2\theta = 90 \sin 2\theta / \mu_{\rm eff} \pi R, \tag{3.3.15}$$

where $\mu_{\rm eff}$ is the effective sample absorption coefficient taking into account the packing density.

3.3.2.4. *Fundamental parameters profile modelling*

An alternative method for describing the source and instrumental part of the powder peak profile is to develop a set of individual functions that form the part of the profile arising from each of the instrumental components that shape the beam profile (Cheary & Coelho, 1992, 1998*a*,*b*). Ideally, each function is parameterized in terms of the physical parameters of the corresponding instrument component (*e.g.* slit width and height, sample dimensions and absorption, source size and emission characteristics, *etc.*), which are known from direct measurement. The set of functions are then convoluted *via* fast mathematical procedures to produce a line profile that matches the observed one. Any remaining profile-broadening parameters (*e.g.* for sample crystallite size and microstrain, see Section 3.3.5 for details) are then allowed to adjust during a Rietveld refinement. By employing this fundamental parameters (FP) approach, these parameters are unaffected by any instrumental parameterization.

The FP method offers two clear advantages over the more empirical approach outlined in Sections 3.3.2.1–3.3.2.3 above: (i) it can more closely describe the actual instrumental effects that contribute to the profile shape, thus improving the precision of the fit to the observed data and (ii) it can be used to describe a source characteristic or an instrumental arrangement that is outside the normally used configuration, yielding a result that would be difficult to obtain otherwise (Cheary *et al.*, 2004).

3.3.3. Peak profiles for neutron time-of-flight experiments

3.3.3.1. *The experiment*

The neutron source in a time-of-flight (TOF) powder diffraction experiment produces pulses of polychromatic neutrons; these travel over the distance from the source to the sample and then to the detectors which are placed at fixed scattering angles about the sample position; the travel times are of the order of 1–100 ms. This has been briefly described in Volume C of *International Tables for Crystallography* (Jorgensen *et al.*, 1992). Because neutrons of differing velocities (v) have differing wavelengths (λ) according to the de Broglie relationship ($\lambda = h/mv$) given Planck's constant (h) and the neutron mass (m), they will sort themselves out in their time of arrival at the detector. The powder pattern appears as a function of TOF *via* Bragg's law ($\lambda = 2d\sin\theta$) in which the wavelength is varied and θ is fixed. The approximate relationship between TOF, wavelength and d-spacing observed in a particular detector can be derived from the de Broglie relationship and Bragg's law to give

$$\mathrm{TOF} = 252.7784 L\lambda = 505.5568 L d \sin\theta. \tag{3.3.16}$$

The constants are such that given λ in ångströms and the total neutron flight path length L in metres, then the TOF will be in μs. An analysis of the possible variances in these components then gives an estimate of the powder diffraction peak widths:

$$\Delta d/d = [(\Delta t/t)^2 + (\Delta\theta \cot\theta)^2 + (\Delta L/L)^2]^{1/2}, \tag{3.3.17}$$

where Δd, Δt, $\Delta\theta$ and ΔL are, respectively, the uncertainties in d-spacing, TOF, scattering angle θ and total flight path L (Jorgensen & Rotella, 1982). Consequently, these three terms also determine the instrumental contribution to the neutron TOF powder peak profile.

3.3.3.2. *The neutron pulse shape*

The neutron pulse shape depends on the mode of production. Early studies (Buras & Holas, 1968; Turberfield, 1970) used one or more choppers to define a polychromatic pulse from a reactor source, resulting in essentially Gaussian powder peak profiles whose FWHM (Γ_G) is nearly constant ($B \simeq 0$):

$$\Gamma_G^2 = A + Bd^2, \tag{3.3.18}$$

so that the Rietveld technique can easily be used (*e.g.* Worlton *et al.*, 1976). Unfortunately, this approach gave very low intensities and relatively low resolution powder patterns.

A more useful approach uses a spallation source to produce the pulsed neutron beam. Neutrons are produced when a high-energy proton beam (>500 MeV) strikes a heavy metal target (usually W, U or liquid Hg) *via* a spallation process (Carpenter *et al.*, 1984). These very high energy neutrons strike small containers of moderating material (usually H_2O, liquid CH_4 or liquid H_2) which then comprise the neutron source seen by the powder diffraction instrument. The entire target/moderator system is encased in a neutron-reflective material (usually Be) to enhance the neutron flux and then further encased in a biological shield. Each moderator may be encased on the sides away from the instrument (*e.g.* powder diffractometer) in a thin neutron absorber (*e.g.* Cd or Gd) and may also contain an inner absorber layer ('poison') to sharpen the resulting pulse of thermal neutrons. These sources produce a polychromatic neutron beam that is rich in both thermal (<300 meV) and epithermal (>300 meV) neutrons. The proton pulses can have a very short duration (~200 ns) (from a 'short-pulse' source, *e.g.* ISIS, Rutherford Laboratory, UK or LANSCE, Los Alamos National Laboratory, USA) or a much longer duration (>500 ns) (a 'long-pulse' source, *e.g.* SNS, Oak Ridge National Laboratory, USA or ESS, European Spallation Source, Sweden); the pulse repetition rate at these sources is 10–60 Hz. These characteristics are largely dictated by the proton accelerator and neutron source design. The resulting neutron pulse results from complex down-scattering and thermalization processes in the whole target/moderator assembly; it may be further shaped by choppers,

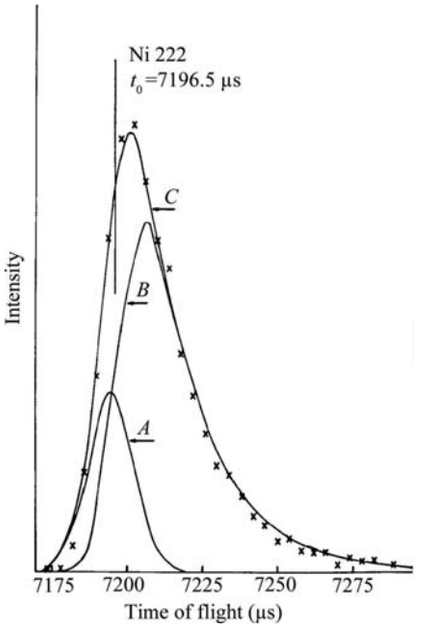

Figure 3.3.3
The observed and calculated Ni 222 diffraction line profile from the Back Scattering Spectrometer, Harwell Laboratory, Chilton, UK. The curves *A* and *B* are computed from the two terms in equation (3.3.19) and curve *C* is the sum (from Von Dreele *et al.*, 1982).

particularly for long-pulse sources, to give what is seen at the powder diffractometer.

Consequently, the neutron pulse structure from these sources has a complex and asymmetric shape, usually characterized by a very sharp rise and a slower decay, both of which are dependent on the neutron wavelength. The resulting powder diffraction peak profile (Fig. 3.3.3) is then the convolution [equation (3.3.2)] of this pulse shape (G_λ) with symmetric functions (G_I) arising from beamline components (*e.g.* slits and choppers) and the sample characteristics (G_S).

3.3.3.3. *The neutron TOF powder peak profile*

An early attempt at representing the TOF peak profile used a piecewise approach combining a leading-edge Gaussian, a peak-top Gaussian and an exponential decay for the tail (Cole & Windsor, 1980). Although single peaks could be fitted well with this function, the variation with TOF was complex and required many arbitrary coefficients.

A more successful approach empirically represented the pulse shape by a pair of back-to-back exponentials which were then convoluted with a Gaussian (Jorgensen *et al.*, 1978; Von Dreele *et al.*, 1982) to give

$$P(\Delta) = \frac{\alpha\beta}{\alpha+\beta}\left\{\exp\left[\frac{\alpha}{2}(\alpha\sigma^2+2\Delta)\right]\operatorname{erfc}\left[\frac{\alpha\sigma^2+\Delta}{\sigma(2^{1/2})}\right] + \exp\left[\frac{\beta}{2}(\beta\sigma^2-2\Delta)\right]\operatorname{erfc}\left[\frac{\beta\sigma^2-\Delta}{\sigma(2^{1/2})}\right]\right\}, \tag{3.3.19}$$

where α and β are, respectively, the coefficients for the exponential rise and decay functions; erfc is the complementary error function. Analysis of the data that were available then gave empirical relations for α, β and σ as

$$\alpha = \alpha_1/d; \quad \beta = \beta_0 + (\beta_1/d^4); \quad \sigma = \sigma_1 d. \tag{3.3.20}$$

The two terms in this function are shown in Fig. 3.3.3. The junction of the two exponentials defines the peak position (shown as a vertical line in Fig. 3.3.3); it is offset to the low side of the peak maximum. This arbitrary choice of peak position then affects the relationship between the TOF and reflection *d*-spacing; an empirical relationship (Von Dreele *et al.*, 1982) was found to suffice:

$$\mathrm{TOF} = Cd + Ad^2 + Z, \tag{3.3.21}$$

with three adjustable coefficients (C, A, Z) established *via* fitting to the pattern from a standard reference material.

Although this profile description was adequate for room-temperature moderators (H_2O or polyethylene) at low-power spallation sources, it does not describe well the wavelength dependence for cold moderators feeding neutron guides used at higher-power sources. An alternative description, employing a switch function to account for the fundamental change in the neutron leakage profile from the moderator between epithermal and thermal neutrons, was proposed (Ikeda & Carpenter, 1985; Robinson & Carpenter, 1990) to accommodate the profiles seen from liquid CH_4 or H_2 moderators. A drawback of this description is that the pulse profile is defined with the peak position at the low TOF edge; convolution with G_I and G_S results in a function where the peak position is far below the peak top. An empirical approach by Avdeev *et al.* (2007) simply requires tables to be established from individual peak fits to a standard material powder pattern for the values of α, β and TOF in place of the expressions given in equations (3.3.20) and (3.3.21); this establishes the G_λ and G_I contributions to the TOF line shape. More recently, some simple extensions (Toby & Von Dreele, 2013) to the empirical functions [equations (3.3.22) and (3.3.23)] appear to better cover the deviations arising from the enhanced epithermal contribution to the cold moderator spectrum:

$$\mathrm{TOF} = Cd + Ad^2 + B/d + Z, \tag{3.3.22}$$

$$\alpha = \frac{\alpha_1}{d}; \quad \beta = \beta_0 + \frac{\beta_1}{d^4} + \frac{\beta_2}{d^2}; \quad \sigma = \sigma_0 + \sigma_1 d^2 + \sigma_2 d^4 + \frac{\sigma_3}{d^2}. \tag{3.3.23}$$

3.3.4. Peak profiles for X-ray energy-dispersive experiments

In an X-ray dispersive powder diffraction experiment, a detector with good energy-discrimination capability is placed at a fixed scattering angle while the sample is illuminated by a 'white' beam of radiation. The detector response is binned into discrete energies by a multichannel analyser (MCA) (Glazer *et al.*, 1978). Typically these instruments display peaks that are purely Gaussian in shape with quite low resolution ($\Delta E/E \simeq 1\%$) and have widths that are proportional to the energy:

$$\Gamma_G = UE + W. \tag{3.3.24}$$

This is most useful for experiments with very limited angular access (*e.g.* high-pressure multi-anvil setups, as described in Chapter 2.7) using synchrotron radiation and can give very high data collection rates on very small samples. Glazer *et al.* (1978) showed that simple crystal structures can be modelled with the Rietveld technique after suitable corrections to account for the variation in source intensity, detector response and sample absorption effects. Otto (1997) expanded the peak-profile description to include possible sample-broadening effects *via* a Voigt profile; this extended the expression in equation (3.3.24) by adding a second-order term in energy and allowed extraction of

size and microstrain sample-broadening effects in cases where these were large.

A related alternative technique (Wang *et al.*, 2004) collects multiple energy-dispersive powder patterns over a narrow and coarse angular step scan; this is easily done in a typical multi-anvil high-pressure setup. The array of spectra are binned as multiple angle-dispersive patterns which are then combined into a single refinement; the complex corrections required for pure energy-dispersive patterns reduce to refinable scaling factors. Typically a scan over 10° 2θ with 0.1–0.2° steps suffices to give suitable data; binning into $\Delta E/E \simeq 20\%$ energy bands gives data that are used in a conventional multiple-data-set Rietveld refinement.

3.3.5. Sample broadening

Very often, particularly for synchrotron-radiation experiments, the powder diffraction peak profile is dominated by broadening effects from the sample, *e.g.*

$$P(\Delta) = G_\lambda * G_I * G_S \simeq G_S. \tag{3.3.25}$$

For the cases considered here, the focus will be on sample-broadening models that allow improved fits within the context of a Rietveld refinement; a more detailed treatment aimed at extracting sample characteristics (*e.g.* crystallite size distributions) is covered in Chapter 5.1.

Two mechanisms for sample broadening are considered here: crystallite size and 'microstrain' broadening; each will be discussed in turn.

3.3.5.1. *Crystallite size broadening*

The reciprocal space associated with an ideal large crystal will consist of a periodic array of infinitely sharp δ functions, one for each of the structure factors, as expected from the Fourier transform of the essentially infinite and periodic crystal lattice. For real crystals, this limit is reached for crystal dimensions exceeding *circa* 10 μm. The Fourier transform of a crystal lattice that is smaller than this will show a profile that follows the form described by the $\mathrm{sinc}(x) = \sin(\pi x)/\pi x$ function. Any dispersion in the crystal sizes in a powder sample will smear this into a form intermediate between a Gaussian and a Lorentzian, which is well described by either a Voigt [equation (3.3.9)], a pseudo-Voigt [equation (3.3.8)] or the less-useful Pearson VII [equation (3.3.7)] function. The physical process used to form the powder will influence the details of the size distribution; usually this will approximate a log-normal distribution and the resulting peak-shape contribution from crystallite size effects will be largely Lorentzian with a width Γ_{SL}. Predominantly Gaussian size broadening can only occur if the size distribution is very tightly monodisperse. Then, for isotropic crystal dimensions this broadening is uniformly the same everywhere in reciprocal space; *e.g.* Δd^* = constant $\simeq 1/p$, where p is the crystallite size. Transformation *via* Bragg's law to the typical measurement of a powder pattern as a function of 2θ gives this Lorentzian width as

$$\Gamma_{pL} = \frac{180}{\pi}\frac{K\lambda}{p\cos\theta} \tag{3.3.26}$$

expressed in degrees and the Scherrer constant, K, which depends on the shape of the crystallites; *e.g.* K = 1 for spheres, 0.89 for cubes *etc.* (see Table 5.1.1 in Chapter 5.1). A similar expression for the crystallite size from a neutron TOF experiment is

$$\Gamma_{pL} = \frac{CK}{p}, \tag{3.3.27}$$

where C is defined by equation (3.3.21). In some cases the crystallites have anisotropic shapes (*e.g.* plates or needles), in which case the peak broadening will be dependent on the respective direction in reciprocal space for each reflection. Many Rietveld refinement programs implement various models for this anisotropy.

3.3.5.2. *Microstrain broadening*

The existence of imperfections (*e.g.* deformation faults) within the crystal lattice produces local distortions of the lattice and thus a broadening of the points in reciprocal space. To a first approximation these points are broadened proportionally to their distance from the origin, *e.g.* $\Delta d^*/d^* = \Delta d/d \simeq$ constant.

As for crystallite size, there is normally dispersion in the density of defects and thus the peak shape will be intermediate between a Gaussian and a Lorentzian form, and it is well described by the Voigt, pseudo-Voigt or Pearson VII functions. Usually, the Lorentzian form dominates this type of broadening and it is the most common form of sample broadening in powder diffraction. It usually arises because of defects introduced during sample preparation (especially during grinding). The Lorentzian width contribution from microstrain broadening is

$$\Gamma_{sL} = \frac{180}{\pi} s \tan\theta, \tag{3.3.28}$$

where s is the dimensionless microstrain; it is frequently multiplied by 10^6. A similar expression for neutron TOF is

$$\Gamma_{sL} = Csd, \tag{3.3.29}$$

where C is defined by equation (3.3.21).

In many cases, the microstrain broadening is not isotropic; presumably this is a consequence of the interaction between the defects and the elastic properties of the crystals. A phenomenological description of these effects by Popa (1998) and Stephens (1999) is obtained by considering the variance of

$$\frac{1}{d^2} = M_{hkl} = \alpha_1 h^2 + \alpha_2 k^2 + \alpha_3 l^2 + \alpha_4 kl + \alpha_5 hl + \alpha_6 hk \tag{3.3.30}$$

with respect to each of the coefficients α_i.

$$\Gamma_{sL}^2 = \sum_{i,j} S_{ij} \frac{\partial M}{\partial \alpha_i}\frac{\partial M}{\partial \alpha_j} \tag{3.3.31}$$

where

$$\frac{\partial M}{\partial \alpha_i}\frac{\partial M}{\partial \alpha_j} = \begin{bmatrix} h^4 & h^2k^2 & h^2l^2 & h^2kl & h^3l & h^3k \\ h^2k^2 & k^4 & k^2l^2 & k^3l & hk^2l & hk^3 \\ h^2l^2 & k^2l^2 & l^4 & kl^3 & hl^3 & hkl^2 \\ h^2kl & k^3l & kl^3 & k^2l^2 & hkl^2 & hk^2l \\ h^3l & hk^2l & hl^3 & hkl^2 & h^2l^2 & h^2kl \\ h^3k & hk^3 & hkl^2 & hk^2l & h^2kl & h^2k^2 \end{bmatrix}. \tag{3.3.32}$$

Examination of this sum for the triclinic case collects terms to give

$$\begin{aligned}\Gamma_{sL}^2 = {} & S_{400}h^4 + S_{040}k^4 + S_{004}l^4 + 3(S_{220}h^2k^2 + S_{202}h^2l^2 + S_{022}k^2l^2) \\ & + 2(S_{310}h^3k + S_{103}hl^3 + S_{031}k^3l + S_{130}hk^3 + S_{301}h^3l + S_{013}kl^3) \\ & + 4(S_{211}h^2kl + S_{121}hk^2l + S_{112}hkl^2)\end{aligned} \tag{3.3.33}$$

with 15 coefficients S_{hkl}. The subscript hkl in S_{hkl} refers to the powers used for h, k, l in equations (3.3.33)–(3.3.44).

For Laue symmetries other than triclinic, there are restrictions on the allowed S_{hkl} terms and, as a practical matter, additional equivalences from symmetry-forced reflection overlaps for trigonal and tetragonal Laue symmetries.

Monoclinic (2/m, b axis unique; others similar, nine coefficients):

$$\Gamma_{sL}^2 = S_{400}h^4 + S_{040}k^4 + S_{004}l^4 + 3S_{202}h^2l^2 + 3(S_{220}h^2k^2 + S_{022}k^2l^2) + 2(S_{301}h^3l + S_{103}hl^3) + 4S_{121}hk^2l. \quad (3.3.34)$$

Orthorhombic (mmm, six coefficients):

$$\Gamma_{sL}^2 = S_{400}h^4 + S_{040}k^4 + S_{004}l^4 + 3(S_{220}h^2k^2 + S_{202}h^2l^2 + S_{022}k^2l^2). \quad (3.3.35)$$

Tetragonal (4/m, five coefficients):

$$\Gamma_{sL}^2 = S_{400}(h^4 + k^4) + S_{004}l^4 + 3S_{220}h^2k^2 + 3S_{202}(h^2l^2 + k^2l^2) + 2S_{310}(h^3k - hk^3). \quad (3.3.36)$$

The last coefficient (S_{310}) cannot normally be determined owing to exact reflection overlaps. Thus, equation (3.3.37) is normally used for both 4/m and 4/mmm Laue symmetries:

Tetragonal (4/mmm, four coefficients):

$$\Gamma_{sL}^2 = S_{400}(h^4 + k^4) + S_{004}l^4 + 3S_{220}h^2k^2 + 3S_{202}(h^2l^2 + k^2l^2). \quad (3.3.37)$$

Trigonal ($\bar{3}$, rhombohedral setting, five coefficients):

$$\Gamma_{sL}^2 = S_{400}(h^4 + k^4 + l^4) + 3S_{220}(h^2k^2 + h^2l^2 + k^2l^2) + 2S_{310}(h^3k + k^3l + hl^3) + 2S_{130}(h^3l + kl^3 + hl^3) + 4S_{211}(h^2kl + hk^2l + hkl^2). \quad (3.3.38)$$

The pair of coefficients S_{310} and S_{130} cannot normally be independently determined owing to exact reflection overlaps. Thus, equation (3.3.39) is normally used for both rhombohedral symmetries:

Trigonal ($\bar{3}m$, rhombohedral setting, four coefficients):

$$\Gamma_{sL}^2 = S_{400}(h^4 + k^4 + l^4) + 3S_{220}(h^2k^2 + h^2l^2 + k^2l^2) + 2S_{310}(h^3k + k^3l + hl^3 + h^3l + kl^3 + hl^3) + 4S_{211}(h^2kl + hk^2l + hkl^2). \quad (3.3.39)$$

Trigonal ($\bar{3}$, five coefficients):

$$\Gamma_{sL}^2 = S_{400}(h^4 + k^4 + 2h^3k + 2hk^3 + 3h^2k^2) + S_{004}l^4 + 3S_{202}(h^2l^2 + k^2l^2 + hkl^2) + S_{301}(2h^3l - 2k^3l - 6hk^2l) + 4S_{211}(h^2kl + hk^2l). \quad (3.3.40)$$

The coefficient S_{301} cannot normally be independently determined owing to exact reflection overlaps. Thus, equation (3.3.42) is normally used for $\bar{3}$ Laue symmetry.

Trigonal ($\bar{3}m1$, four coefficients):

$$\Gamma_{sL}^2 = S_{400}(h^4 + k^4 + 2h^3k + 2hk^3 + 3h^2k^2) + S_{004}l^4 + 3S_{202}(h^2l^2 + k^2l^2 + hkl^2) + S_{301}(3h^2kl - 3hk^2l + 2h^3l - 2k^3l). \quad (3.3.41)$$

The coefficient S_{301} cannot normally be independently determined due to exact reflection overlaps. Thus, equation (3.3.43) is normally used for $\bar{3}m1$ Laue symmetry.

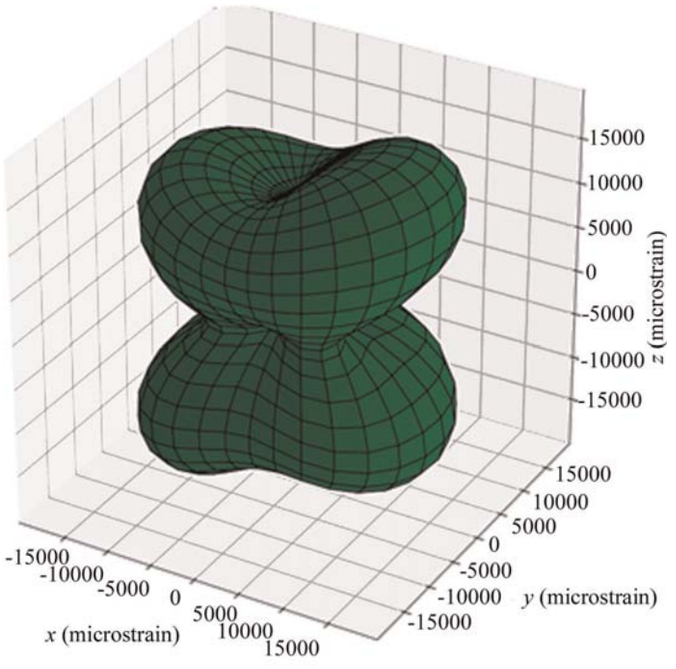

Figure 3.3.4
Microstrain surface for sodium parahydroxybenzoate multiplied by 10^6.

Trigonal ($\bar{3}1m$, four coefficients):

$$\Gamma_{sL}^2 = S_{400}(h^4 + k^4 + 2h^3k + 2hk^3 + 3h^2k^2) + S_{004}l^4 + 3S_{202}(h^2l^2 + k^2l^2 + hkl^2) + 4S_{211}(h^2kl + hk^2l). \quad (3.3.42)$$

Hexagonal (6/m and 6/mmm, three coefficients):

$$\Gamma_{sL}^2 = S_{400}(h^4 + k^4 + 2h^3k + 2hk^3 + 3h^2k^2) + S_{004}l^4 + 3S_{202}(h^2l^2 + k^2l^2 + hkl^2). \quad (3.3.43)$$

Cubic ($m\bar{3}$ and $m\bar{3}m$, two coefficients):

$$\Gamma_{sL}^2 = S_{400}(h^4 + k^4 + l^4) + 3S_{220}(h^2k^2 + h^2l^2 + k^2l^2). \quad (3.3.44)$$

These equations can be used with the refined values of the coefficients to produce a surface representing the extent of the microstrain in reciprocal space. The surface resulting from Stephens' (1999) analysis of powder diffraction data from sodium parahydroxybenzoate is shown Fig. 3.3.4. At the present time, the connection between the elastic properties and defects with these microstrain surface models is unclear. Some aspects of this for cubic and hexagonal systems are discussed in Chapter 5.1.

References

Avdeev, M., Jorgensen, J., Short, S. & Von Dreele, R. B. (2007). *On the numerical corrections of time-of-flight neutron powder diffraction data. J. Appl. Cryst.* **40**, 710–715.

Buras, B. & Holas, A. (1968). *Nukleonika*, **13**, 591–620.

Caglioti, G., Paoletti, A. & Ricci, F. P. (1958). *Choice of collimators for a crystal spectrometer for neutron diffraction. Nucl. Instrum.* **3**, 223–228.

Carpenter, J. M., Lander, G. H. & Windsor, C. G. (1984). *Instrumentation at pulsed neutron sources. Rev. Sci. Instrum.* **55**, 1019–1043.

Cheary, R. W. & Coelho, A. A. (1998*a*). *Axial divergence in a conventional X-ray powder diffractometer. I. Theoretical foundations. J. Appl. Cryst.* **31**, 851–861.

Cheary, R. W. & Coelho, A. A. (1998*b*). *Axial divergence in a conventional X-ray powder diffractometer. II. Realization and evalua-*

tion in a fundamental-parameter profile fitting procedure. J. Appl. Cryst. **31**, 862–868.
Cheary, R. W. & Coelho, A. (1992). *A fundamental parameters approach to X-ray line-profile fitting. J. Appl. Cryst.* **25**, 109–121.
Cheary, R. W., Coelho, A. A. & Cline, J. P. (2004). *Fundamental parameters line profile fitting in laboratory diffractometers. J. Res. Natl Inst. Stand. Technol.* **109**, 1–25.
Cole, I. & Windsor, C. G. (1980). *The lineshapes in pulsed neutron powder diffraction. Nucl. Instrum. Methods*, **171**, 107–113.
Cooper, M. J. & Sayer, J. P. (1975). *The asymmetry of neutron powder diffraction peaks. J. Appl. Cryst.* **8**, 615–618.
David, W. I. F. (1986). *Powder diffraction peak shapes. Parameterization of the pseudo-Voigt as a Voigt function. J. Appl. Cryst.* **19**, 63–64.
Finger, L. W., Cox, D. E. & Jephcoat, A. P. (1994). *A correction for powder diffraction peak asymmetry due to axial divergence. J. Appl. Cryst.* **27**, 892–900.
Glazer, A. M., Hidaka, M. & Bordas, J. (1978). *Energy-dispersive powder profile refinement using synchrotron radiation. J. Appl. Cryst.* **11**, 165–172.
Hastings, J. B., Thomlinson, W. & Cox, D. E. (1984). *Synchrotron X-ray powder diffraction. J. Appl. Cryst.* **17**, 85–95.
Howard, C. J. (1982). *The approximation of asymmetric neutron powder diffraction peaks by sums of Gaussians. J. Appl. Cryst.* **15**, 615–620.
Ikeda, S. & Carpenter, J. M. (1985). *Wide-energy-range, high-resolution measurements of neutron pulse shapes of polyethylene moderators. Nucl. Instrum. Methods Phys. Res. Sect. A*, **239**, 536–544.
Jorgensen, J. D., David, W. I. F. & Willis, B. T. M. (1992). *White-beam and time-of-flight neutron diffraction*. In *International Tables for Crystallography*, Vol. C, edited by A. J. C. Wilson. Dordrecht: Kluwer.
Jorgensen, J. D., Johnson, D. H., Mueller, M. H., Peterson, S. W., Worlton, J. G. & Von Dreele, R. B. (1978). *Profile analysis of pulsed-source neutron powder diffraction data*. Proceedings of the Conference on Diffraction Profile Analysis, Cracow 14–15 August 1978, pp. 20–22.
Jorgensen, J. D. & Rotella, F. J. (1982). *High-resolution time-of-flight powder diffractometer at the ZING-P″ pulsed neutron source. J. Appl. Cryst.* **15**, 27–34.
Laar, B. van & Yelon, W. B. (1984). *The peak in neutron powder diffraction. J. Appl. Cryst.* **17**, 47–54.
Malmros, G. & Thomas, J. O. (1977). *Least-squares structure refinement based on profile analysis of powder film intensity data measured on an automatic microdensitometer. J. Appl. Cryst.* **10**, 7–11.
Otto, J. W. (1997). *On the peak profiles in energy-dispersive powder X-ray diffraction with synchrotron radiation. J. Appl. Cryst.* **30**, 1008–1015.
Parrish, W. (1992). *Powder and related techniques: X-ray techniques*. In *International Tables for Crystallography*, Vol. C, edited by A. J. C. Wilson, ch. 2.3. Dordrecht: Kluwer.
Popa, N. C. (1998). *The (hkl) dependence of diffraction-line broadening caused by strain and size for all Laue groups in Rietveld refinement. J. Appl. Cryst.* **31**, 176–180.
Rietveld, H. M. (1967). *Line profiles of neutron powder-diffraction peaks for structure refinement. Acta Cryst.* **22**, 151–152.
Rietveld, H. M. (1969). *A profile refinement method for nuclear and magnetic structures. J. Appl. Cryst.* **2**, 65–71.
Robinson, R. A. & Carpenter, J. M. (1990). *On the use of switch functions in describing pulsed moderators*. Report LAUR 90-3125. Los Alamos National Laboratory, USA.
Stephens, P. W. (1999). *Phenomenological model of anisotropic peak broadening in powder diffraction. J. Appl. Cryst.* **32**, 281–289.
Thompson, P., Cox, D. E. & Hastings, J. B. (1987). *Rietveld refinement of Debye–Scherrer synchrotron X-ray data from Al_2O_3. J. Appl. Cryst.* **20**, 79–83.
Toby, B. H. & Von Dreele, R. B. (2013). *GSAS-II: the genesis of a modern open-source all-purpose crystallographic software package. J. Appl. Cryst.* **46**, 544–549.
Turberfield, K. C. (1970). *Time-of-flight neutron diffractometry*. In *Thermal Neutron Diffraction*, edited by B. T. M. Willis. Oxford University Press.
Von Dreele, R. B., Jorgensen, J. D. & Windsor, C. G. (1982). *Rietveld refinement with spallation neutron powder diffraction data. J. Appl. Cryst.* **15**, 581–589.
Wang, Y., Uchida, T., Von Dreele, R., Rivers, M. L., Nishiyama, N., Funakoshi, K., Nozawa, A. & Kaneko, H. (2004). *A new technique for angle-dispersive powder diffraction using an energy-dispersive setup and synchrotron radiation. J. Appl. Cryst.* **37**, 947–956.
Worlton, J. G., Jorgensen, J. D., Beyerlein, R. A. & Decker, D. L. (1976). *Multicomponent profile refinement of time-of-flight neutron diffraction data. Nucl. Instrum. Methods*, **137**, 331–337.
Young, R. A., Mackie, P. E. & von Dreele, R. B. (1977). *Application of the pattern-fitting structure-refinement method of X-ray powder diffractometer patterns. J. Appl. Cryst.* **10**, 262–269.
Young, R. A. & Wiles, D. B. (1982). *Profile shape functions in Rietveld refinements. J. Appl. Cryst.* **15**, 430–438.